Analysis of fiber-matrix interface debonding under normal loading using in-situ microscopy and cruciform-shaped single glass fiber/composite specimens

Olivier Verschatse[1], *Mehdi Nikforooz*[1], *Karen De Clerck*[1], *Wim Van Paepegem*[1] *and Lode Daelemans*[1,*]

[1] *Department of Materials, Textiles and Chemical Engineering (MaTCh), Ghent University, Technologiepark 70A, B-9052 Zwijnaarde, Belgium*

**corresponding author: lode.daelemans@ugent.be*

Abstract

One of the important microscale properties that determine a composite's performance is the fiber-matrix interface strength. Research has primarily been focused on the interface strength under shear loading, while studies on interface strength under normal loading are limited. Nevertheless, normal loading is very relevant, for example to understand failure mechanisms in 90° plies. Therefore, in this work, we modified a single fiber composite test to a cruciform shape with a thinned middle section to test glass fiber matrix interface properties under normal loading conditions. These specimens allow testing the interface up till the point of failure of the polymer matrix, thus improving over regular cruciform specimens. An in-house designed tensile stage enabled the use of in -situ transmission and reflection microscopy. Insights into the debonding process were obtained over a large fiber length (± 10 mm) via the use of a step-and-shoot method. The methodology is applied to a glass fiber with an epoxy compatible and incompatible sizing. It shows that the debonding process can be divided into two partially independent debonding processes (initiation and propagation). The obtained data enabled the construction of a descriptive function for the total debond length of a fiber-matrix interface. This showed that besides a high interface strength, a homogeneous application of the sizing should be aimed to decrease the chances of initiating debonding at lower stresses.

Graphical abstract

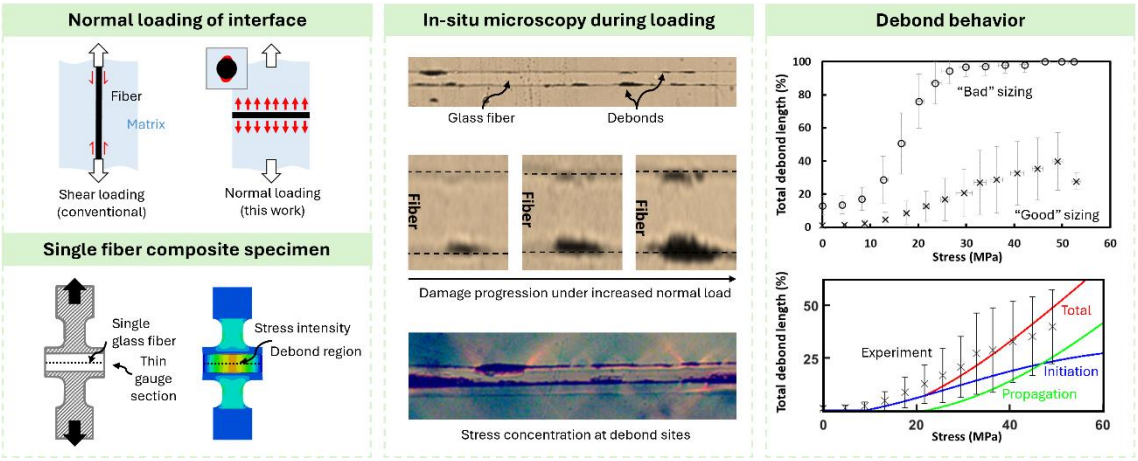

***Keywords*: cruciform, fiber-matrix interaction, debonding, glass fiber**

Highlights:

- Normal loading of single glass fiber/matrix interface using cruciform specimens made using microscale VARI.
- Large interface section is analyzed for initiation and propagation events using a step-and-shoot loading method combined with transmission optical microscopic imaging.
- In-situ results show that debond initiation and propagation are partially independent and coexisting processes.
- A descriptive function was constructed showing the influences of different parameters on the total debonding length of the fiber-matrix interface

1. Introduction

Fiber-reinforced polymer composites are one of the go-to structural materials of the future. Nowadays these materials are already used in many applications such as airplanes, wind turbines, and construction. To achieve optimal properties, the fiber-matrix interface is very important as it dictates how well the load is transferred to the fibers, and how damage initiates and propagates. However, quantifying this property is not straightforward. Yet, obtaining correct information about this property is very important for characterizing composites as well as for the use of numerical multiscale simulations. These simulations enable the prediction of composite behavior and failure on different levels, greatly reducing time and cost for the development of new composite applications

[1–4]. To assure the correctness of numerical predictions, a good understanding of the microscale behavior as well as correct microscale input properties are thus needed.

To evaluate the interface strength a variety of methods can be used [5–9]. Often used methods are the microdroplet test [10–14], the fragmentation test [15–17], and the fiber pull-out test [15,18–20] (**Figure 1**). These tests are used to quantify the fiber-matrix debonding initiation and propagation. Yet, obtaining an absolute quantitative value of the interfacial strength can be difficult as different data reduction schemes are used. This makes these tests useful to compare different treatments with each other, yet limited in obtaining accurate quantitative values [17]. Another downside is their limitation to characterize only the interface strength under shear loading while often a composite fails first in a layer with normal or mixed mode stress at the fiber-matrix interface. To tackle this problem, several other tests were proposed over the years such as the Broutmann test [21–24] and the transverse tensile test [25–29]. These apply load to the interface in the normal direction of the fiber.

The Broutmann test is constructed in such a way that by applying a compressive force on the sample, the transverse fiber-matrix properties can be determined (**Figure 1d**). Due to the Poisson coefficient, the compressive stresses will result in radial tension around the fiber, these stresses will be highest in the necked middle section of the sample. Fiber-matrix debonding will thus occur under transverse stresses. Yet the compressive forces exerted on the material can result in early failure of the sample or fiber. A more direct method to test the normal fiber-matrix interface properties is to perform a transverse tensile test (**Figure 1e**). Therefore a single fiber is embedded in the matrix material and loaded in the transverse direction. The fiber-matrix debonding can be observed both at the edges of the sample or in the middle part. Yet, these free edges result in stress concentrations making those zones more prone to debonding. To prevent premature debonding the cruciform shape was first introduced by Gundel *et al*.[30] The special cruciform shape mitigates the influence of the free fiber edges present in the sample (**Figure 1f**). The whole sample is under a tensile load (normal to the fiber direction) with a decreasing stress level from the middle toward the cruciform arms. Therefore failure of the fiber-matrix interface will first happen in the middle zone of the sample and will progressively grow towards the cruciform arms [31–34].

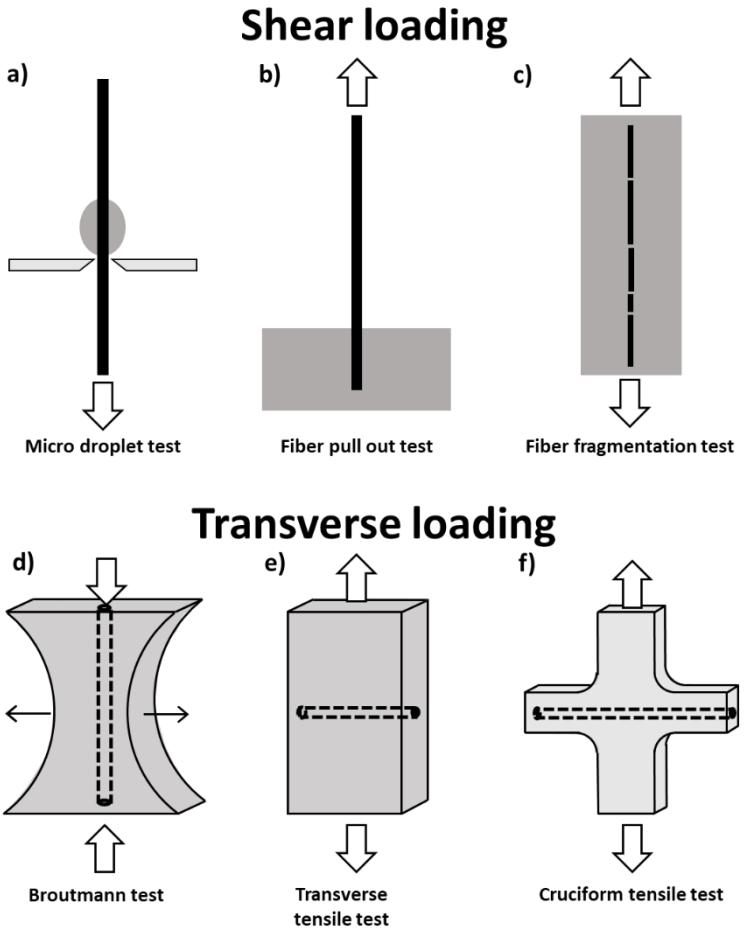

Figure 1 - Schematic overview of the interface strength tests. (a-c) interface shear strength tests and (d-f) interface transverse strength.

Over the years, several researchers have used and altered the cruciform shape to study the debonding behavior under normal loading or a combination of normal and shear loading via altering the angle of the cruciform arms [35–37]. These studies show the great potential for cruciform samples as a method to study the fiber-matrix adhesion strength and failure behavior under transverse loading conditions as well as mixed loading conditions. Via observing the initiation and propagation of the debonding, values for interface strength and energy release rate could be determined. However, up till now, only a limited number of studies are available, and several of these use unsized fibers and/or low-resolution imaging (**Table 1**). This limits the impact of a very promising technique for testing debonding properties under normal stresses.

95 **Table 1 – Overview of research papers on fiber-matrix debonding using cruciform specimens.**

Reference	Fiber / matrix combination	Production method	Observation technique
Gundel et al. [30]	SiC / Ti-6Al-4V	Diffusion bonding	Acoustic emission
Bechel et al. [36]	Carbon / Epoxy	Pouring of degassed resin	Optical microscopy
Tandon et al. [31]	SiC / Epoxy	Pouring of resin	Optical microscopy
Tandon et al. [35]	SiC / Epoxy	Pouring of resin	Optical microscopy
Majumdar et al. [38]	SiC / BSi glass	Sintering of sheets	Post-mortem
Foster et al. [37]	Steel / Epoxy	Pouring of degassed resin	Optical microscopy
Koyanagi et al. [8]	Glass / Epoxy	Pouring of resin	Optical microscopy
Koyanagi et al. [34]	Glass / Epoxy	Pouring of resin	Optical microscopy
Levine et al. [39]	Glass / Epoxy	Degassing of poured resin	High speed camera
Chu et al. [33]	Aramid / Epoxy Glass / Epoxy	Degassing of poured resin	High speed camera

96

97 In this study, we further improved on the production method to obtain thin, void-free
98 samples. This new, vacuum-assisted resin infusion (VARI), high-quality production
99 method was combined with a modified cruciform design to maximize debonding events
100 before matrix failure is encountered. The obtained samples had a nominal thickness of
101 200 µm and enabled clear observation of the debonding process via both normal and
102 polarised light microscopy. The limited thickness also allowed the use of normal
103 microscope objectives (no need for expensive long-working distance objectives) and a
104 light-weight tensile testing machine. The thickness was still sufficient as not too affect
105 the stress concentration field near the fiber. The cruciform samples were subjected to a
106 step-and-shoot method allowing to study of a much larger fiber-matrix interface length
107 throughout a tensile test, gaining new insights into the debond initiation and propagation
108 process. Two identical glass fibers, yet with a different sizing (good/compatible vs.
109 bad/incompatible) were studied to pinpoint differences in the adhesion characteristics.
110 The combination of these innovations led to new insights into the debonding process
111 under normal tension.

112 ## 2. Materials and methods

113 ### *2.1. Materials*

114 The epoxy resin used was Epikote^{TM} Resin MGS RIMR 135, which is based on diglycidyl
115 ether of bisphenol A (DGEBA), combined with a liquid diamine hardener, Epicure^{TM}
116 Curing Agent MGS RIMH 137 obtained from Momentive Specialty Chemicals. Both
117 components were mixed in a 100:30 weight ratio and degassed in a vacuum desiccator

for 10 minutes. After optimal curing, 24h at room temperature followed by 15h at 80°C, this leads to an epoxy system with a Tg between 80 and 90°C. This curing sequence is used for the production of wind turbine blades, making it a relevant process to study.

Two types of E-glass fibers were used which were obtained via Johns Manville. One containing an epoxy-compatible sizing (StarRov® PR 220 1200 090) and one containing an epoxy-incompatible sizing (StarRov® PR 220 1200 490). The fibers have a nominal filament diameter of 16 µm.

2.2. Methods

Whereas in previous research, cruciform samples were made via pouring resin into a mold, whether or not degassed, here a completely sealed mold is used in combination with a miniaturized VARI process. Single-use molds were made with laser cut tape, used as spacers, and two glass plates as top and bottom sides to ensure flat surfaces (**Figure 2**). A single glass fiber was placed between the layers of tape at half the mold thickness. The fibers were preloaded with 50 mg calibration weights, inducing a negligible preload stress of 2–3 MPa, to ensure fiber straightness before infusion. To ensure vacuum, the molds were sealed off via vacuum sealing tape and an in- and outlet tubing was attached. A degassed epoxy resin was subsequently transferred into the mold via the VARI process, this ensures the absence of air gaps in the matrix and at the fiber-matrix interface. After curing the samples were detached from the mold and cleaned with a detergent solution and a microfiber cloth. Specimens exhibiting fiber curvature, infusion defects, or thickness variations were excluded from the analysis. A DSC measurement of the cured sample shows a Tg of 85.3 ± 0.2°C which agrees with the Tg of a completely cured bulk sample confirming that a similar curing degree as for bulkscale samples is achieved.

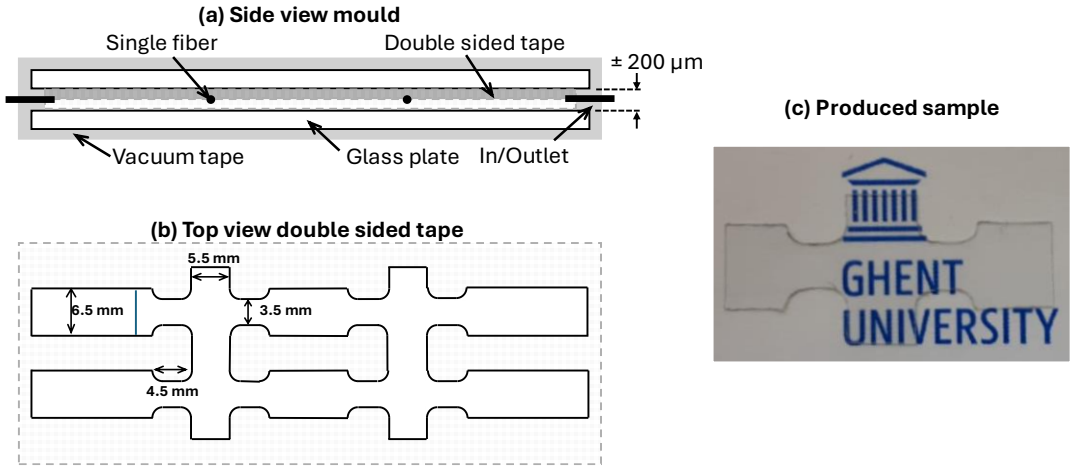

141

142 **Figure 2 - (a) Side view of the constructed mold. (b) Top view of the laser cut double-sided tape used as spacer. (c)**
143 **After unmoulding a transparent sample is obtained.**

144 The specific build-up of the cruciform samples, with a curved transition towards the
145 middle part with the extensive arms, results in a stress concentration at this curved section.
146 This can result in premature fracture of the samples, limiting the attainable stress levels
147 of the fiber-matrix debonding. The addition of a support sheet on the loading arms,
148 increasing the thickness of this fracture-prone zone, can resolve this issue [36]. By
149 applying this thicker zone, a stress concentration in the very middle part of the sample,
150 creating a favorable position for debonding, is achieved. Therefore, supporting tabs were
151 used that thicken the loading arm zone as well as part of the wider zone of the cruciform
152 sample. The supporting tabs (emery paper) were manually applied to the specimens
153 (**Figure 3**). This resulted in a thinned middle section with a nominal thickness of 200 µm
154 (average thickness and standard deviation for all 10 specimens was 186 ± 5 µm), and a
155 nominal gauge area of 3.5 mm x 10 mm, with the fiber located in the middle of this gauge
156 area.

157 A simplified linear elastic finite element model was constructed with the thicker zones
158 conceived as one material (epoxy) (structured mesh, element size of 0.1 mm, quadratic
159 hexahedral elements (C3D20)). The fiber was not incorporated in the model. The model
160 confirms that the highest stresses are present in the center zone of the gauge area and
161 gradually decrease towards the sides of the gauge area (**Figure 3**). Due to the thinner
162 gauge area, stress levels up to around three times those present in the loading arms
163 (nominal stress) are observed. This enables the study of a large area of fiber-matrix
164 interface, while preventing premature failure of the cruciform sample. The use of a linear

elastic model is acceptable as the samples broke at values around 50 MPa in the gauge area of the sample, which is at the edge of the linear elastic zone of the used epoxy. ([40])

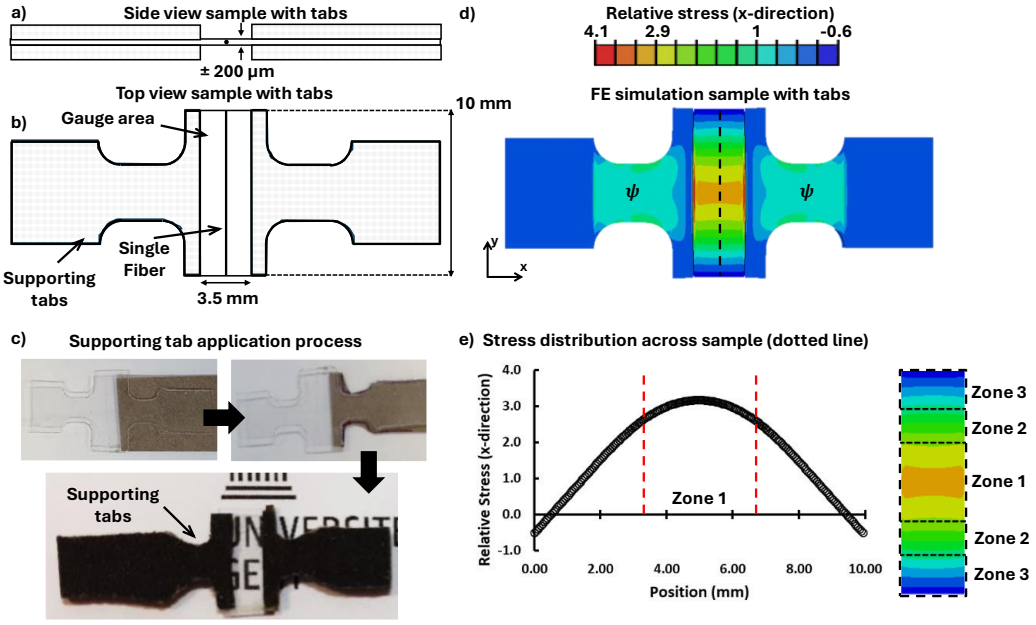

Figure 3 – (a) Side and (b-c) top view of the sample with supporting tabs. (d-e) A Finite elements simulation confirms that the highest stress region is in the middle of the sample. The relative stress factor across the dotted line shows that in 'Zone 1' a relative even stress is present with an average relative stress factor of 3 compared to the loading arms.

Tensile tests (five specimens for each sizing type) were executed on an in-house built tensile stage containing a 100 N loadcell and two-step motors, enabling dual axial displacement (**Figure 4**). A step-and-shoot method with 5 N increments was performed with a displacement speed of 0.75 mm/min for a 15 mm gauge length until fracture occurred. The specimen was loaded to a specific load and then the displacement was held constant. The stress levels shown are those after relaxation.

The stress present in the zone indicated by 'ψ' (nominal stress, **Figure 3d**) is equal to the remotely applied load divided by the cross-sectional area of the loading arm (**Equation 1**).

$$\sigma_{nominal} = \frac{F}{A_{loading\ arm}} \quad (1)$$

The relative scale obtained via the finite element model is used as a correction factor ($f_{gauge\ area}$) to obtain an estimated stress value in the central area near the fiber-matrix interface (thin zone stress) (**Equation 2**). This can be seen as the 'far field' stress around the fiber-matrix interface zone

$$\sigma_{gauge\ area} = f_{gauge\ area} * \sigma_{nominal} \quad (2)$$

Due to the relatively uniform stress distribution in the middle of the thin part section (approximately 3.5 mm in length), a single stress level is used as reference 'far field' stress level. Since local debonding, the exact position of the debond, etc. influence the local stress level at each point along the fiber no local stress levels were calculated or reported and the far field stress is used in the analysis.

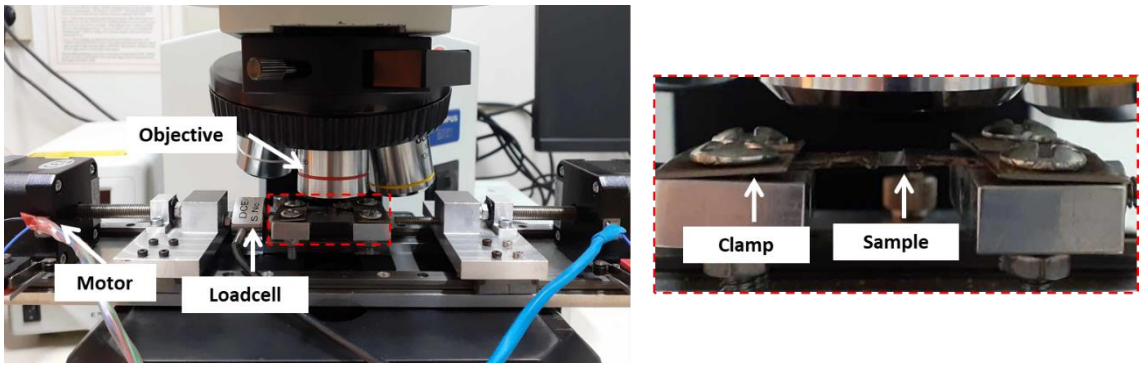

Figure 4 - Overview of the test set-up. An Olympus BX-51 microscope was used with an in-house made dedicated tensile stage. Via transmission lighting (normal and polarized) the sample could be studied.

At each step, the whole width of the cruciform was investigated with an Olympus BX-51 microscope (**Figure 4**). This enabled visualization in both transmission and reflection modes with both normal and polarised light from directly above or below the sample, and not only with angled light as often done in literature. The use of transmission light microscopy visualizes fiber-matrix cracks as fine black lines at the fiber edge (**Figure 5**). While crack growth in the fiber direction will result in longer cracks, radial growth will result in a larger part of the fiber that has become black. The fiber-matrix debonding can also result in the creation of a gap between the fiber and matrix at higher stresses, as a result, the observed black zone will become thicker and grow inwards the matrix zone.

Currently, debond labeling and measurement relied on manual assessment by identifying the dark features. This method, validated by consistent results from both experienced operators and inexperienced users, suggests potential for future automation using image processing techniques, such as thresholding or machine learning, combined with automated optical scanning and stitching via motorized XY-stage movement.

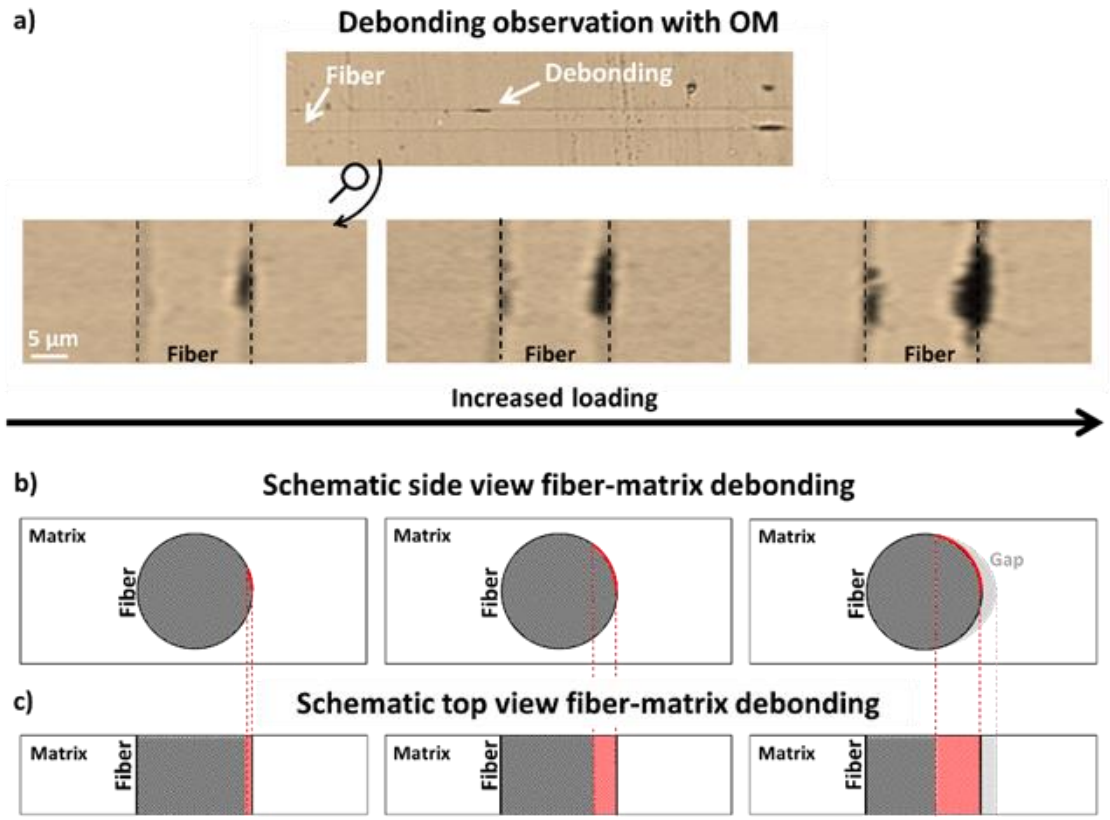

Figure 5 - (a) Fiber-matrix debonding is observed via optical light transmission microscopy as a thin black line at the interface. A closer look reveals that the debond extends in the fiber direction and 'on top of the fiber'. (b-c) A schematic overview shows that the perceived debond growth 'on top of the fiber' is the result of radial debonding and gap opening of the fiber-matrix debonding.

3. Results and discussion

The two differently sized fibers were studied in exactly the same manner, this allows us to compare the debonding process between a compatible and an incompatible sizing. If the method is sensitive to the interface quality, the expectation is to be able to clearly distinguish between both sizings by the measurements and observations.

3.1 Qualitative analysis of the debonding process

For the compatible sized sample, a few debonds along the fiber-matrix interface were observed before the start of the test (**Figure 6a**, 0 MPa). These initial debonds can be due to a multitude of reasons, such as a local absence of sizing agent or the presence of very small defects.

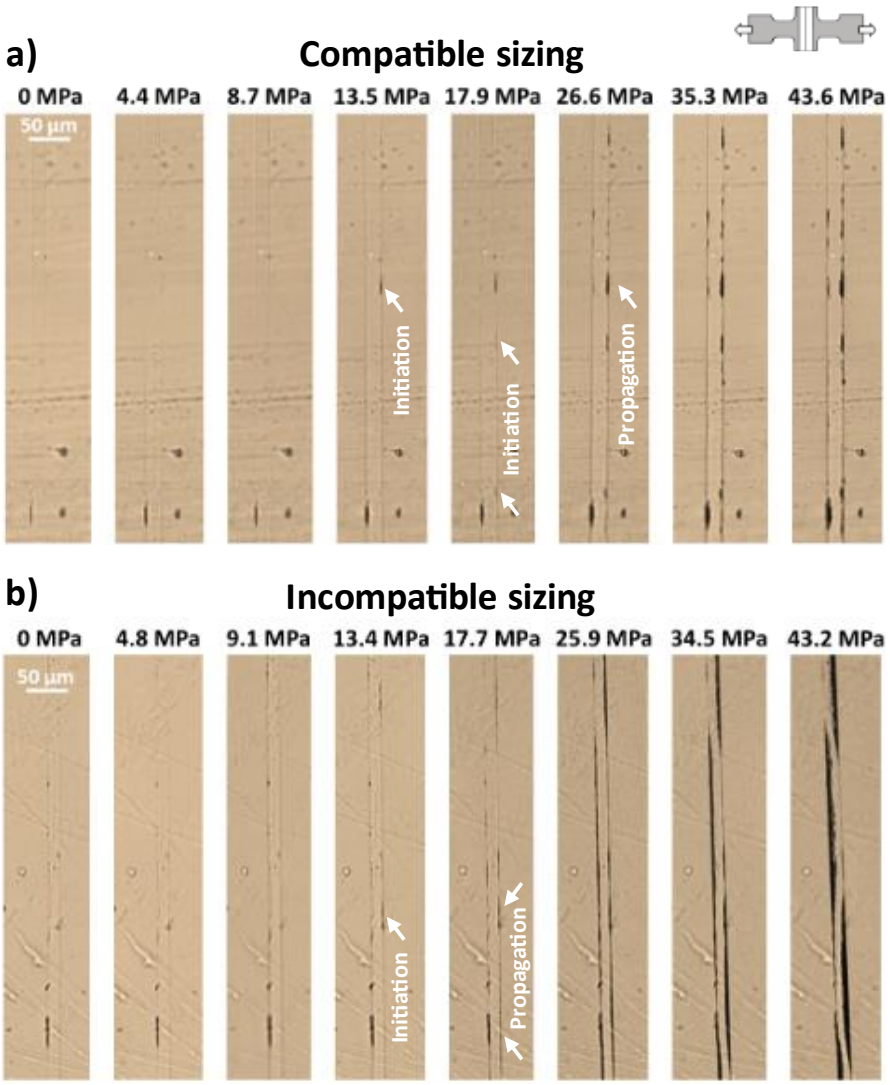

Figure 6 - Observation of the fiber-matrix interface for increasing stress states in the central area of the sample. The creation of new debonds as well as the growth of existing debonds can be observed for both sizings.

Upon loading of the sample, the creation of debonding sites was only observed when a certain stress level was applied to the sample. Once the stress level passes beyond this 'onset of debond initiation' stress, small debonds start to appear at the fiber-matrix interface (**Figure 6a,** 8.7 - 13.5 MPa). The first debonds appear at rather low stress levels for a sizing compatible with the matrix material.

From this point onward new debonds are created with increasing stress level. Yet, the existing debonds do not seem to grow in the fiber direction or only very limited (**Figure 6a**, 26.6 MPa). At the same time, only limited radial growth is observed (wider black spots on fiber). Upon further stress increase local debond growth is observed (**Figure 7a**), while in other spots almost no new debonds nor growth is observed (**Figure 6a,** 35.3 – 43.6 MPa).

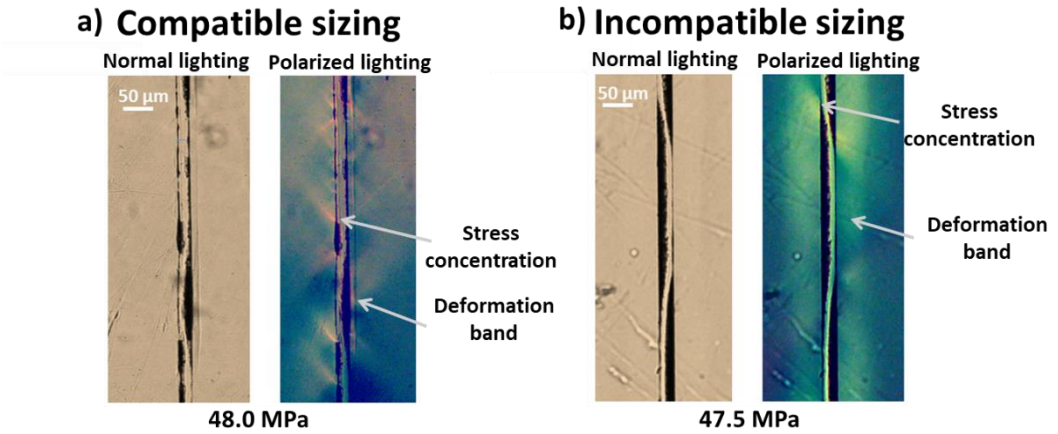

Figure 7 - Plastic deformation and stress concentrations observed around the debonded areas. For both sizings stress concentrations are observed at the tips of the debonds as bright lines under a 45° angle using polarized light. Around the debonded zones a bright zone is observed using polarized lighting, likely indicating plastic deformation. The observed phenomena are much more pronounced for the incompatible sizing samples. Under normal lighting conditions, the phenomena are only faintly visible.

Around the debonded zones, a matrix region with high contrast is observed when polarized transmission microscopy is used (**Figure 7a**). This might be induced by local plasticity. These regions only occur where the fiber has (partially) debonded from the matrix. Indeed, for the compatible sizing, these high-deformation zones are only situated next to debonded zones (**Figure 7a**).

Similar to the compatible-sized samples, the incompatible-sized ones had several debonds before the test was started (**Figure 6b**, 0 MPa). Upon stress increase, debonds start to initiate. Remarkable is that also for the incompatible sized samples a threshold value for debond initiation seems present, and is situated at similar stress levels as the compatible-sized samples (8 - 9 MPa). This suggests that the debonding initiation is at least partially independent from the used sizing and that other factors are in play, because even for the incompatible sizing a 'no initiation' stress zone seems present. Several researchers have suggested that the epoxy shrinkage during cure and the mismatch in thermal expansion coefficient between the matrix and reinforcing fibers result in the presence of a radial compression at the fiber-matrix interface zone [41–45]. This radial compression can result in the delay of debonding initiations, even when a bad sizing is applied. As the fiber and matrix material are identical for both type of specimens, this residual stress will also be similar. The results indicate that a remote stress level of approximately 8 to 10 MPa is required in this case to relieve this residual stress and to allow debond initiation. A similar behavior was observed in our work on short fibers [46,47].

With increasing stress levels, the creation of new debond sites is also observed for the incompatible sizing, while almost at the same time, the growth of the already present debonds is accelerating (**Figure 6b**, 13.4 MPa), in contrast to the compatible sized samples. The growth of the debonds is mainly in the longitudinal direction, while almost no radial growth is observed. Only at a later stage, when already a major part of the interface has debonded, radial growth of the debonds is observed (**Figure 6b**, 32 MPa).

Near the point of failure (>40 MPa), the incompatible-sized fiber is completely debonded from the matrix, while also gap opening is observed. Polarised light microscopy shows that around the fiber a large deformation zone is present (**Figure 7b**). In contrast to the compatible sized samples, almost no stress concentrations at debond tips are observed, while a wider 'deformed' zone is present. Yet, a rather uniform deformation zone is present supporting the observation that the complete fiber has debonded.

The extensive debonding in the incompatible-sized samples resulted in failure at the fiber-matrix interface. This is reflected in the observation of the detached fiber from the matrix at break (**Figure 8b**). In contrast, the compatible-sized samples fail at the edge of the tabs (**Figure 8a**) as the sharp thickness reduction results in a local stress concentration (**Figure 3d**). For both samples, this happened at far field stresses around 50 MPa.

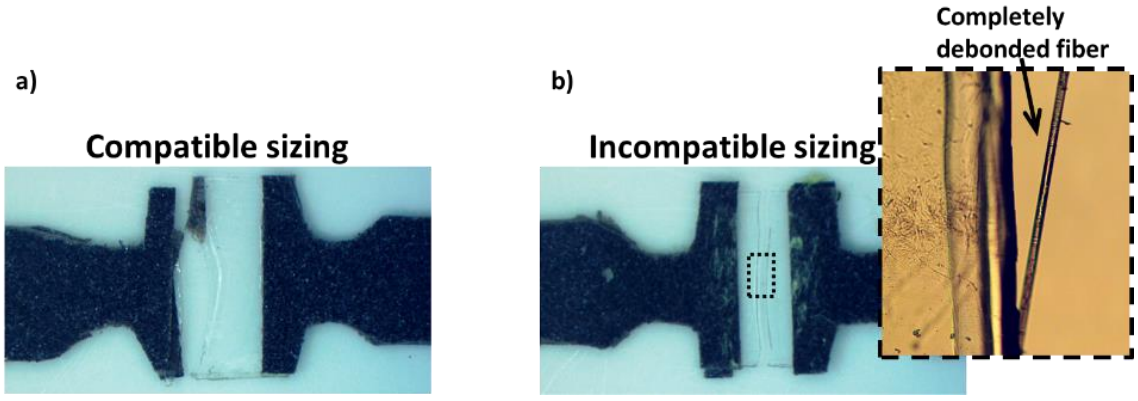

Figure 8 – (a) The compatible-sized fiber samples break at a location away from the fiber-matrix interface, (b) while the incompatible-sized samples break at the interface.

3.2 Quantitative analysis of the debonding process

To get a more quantitative view of the debonding process, the entire length of the fiber was analyzed for debonding observations. At each stress step, images were recorded over the full fiber length, and the following values were determined:

- the number of debonds,

- the (longitudinal) length of each individual debond,
- the zone in which the debond occurred,
- the total debond length as the sum of each individual debond length (absolute and relative to the full interface length),
- the average debond length as the total debond length divided by the number of debonds.

The specific construction of the cruciform sample results in a stress concentration in the middle section of the gauge area and a decrease in stress level towards the sides (**Figure 3e**). This means that towards the edges of the gauge area, the fiber-matrix debonding will be delayed. To have a more accurate/correct view of the debonding phenomena and accompanying stress levels, the stress distribution present in the gauge area needs to be taken into account. Therefore, the gauge area is divided into three zones. The middle zone of the gauge area (± 3.5 mm in length), situated between the loading arms, has a relatively even stress distribution (**Figure 3e**). Outside this middle zone, the stress rapidly lowers towards the edges of the sample. Therefore, the quantitative analysis was focused on zone 1.

Within one sample as well as between different samples with the same sizing type differences in initiation and propagation were observed. This is reflected in relatively high standard deviations (**Figure 9**). Nevertheless, general trends can be observed. The statistical nature of debonding phenomena is likely also reflecting the reality in real-life composites.

As observed in **Figure 6**, the compatible and incompatible-sized samples have a similar initial behavior. In both cases, small debonds are present from the start (**Figure 9c**, 15.0 ± 6.1 µm and 29.0 ± 11.2 µm for the compatible and incompatible sizing respectively). These pretest debonds are spread across the sample. More widespread initial damage is present in the incompatible-sized samples as well as a wider variety between individual samples (**Figure 9a**, 1.2 ± 1.0 % of total length for the compatible sizing versus 13.3 ± 5.6% of total length for the incompatible sizing). These initial debonds can be due to a multitude of reasons, such as a local absence of sizing agent, bad adhesion, or the presence of small defects. The extent of interfacial debonding varies from fiber to fiber, yet all fibers suffer from at least some small debonds. This suggests that such microscale

debonds will also be present in full-scale composite and thus are an inherent part of a composite.

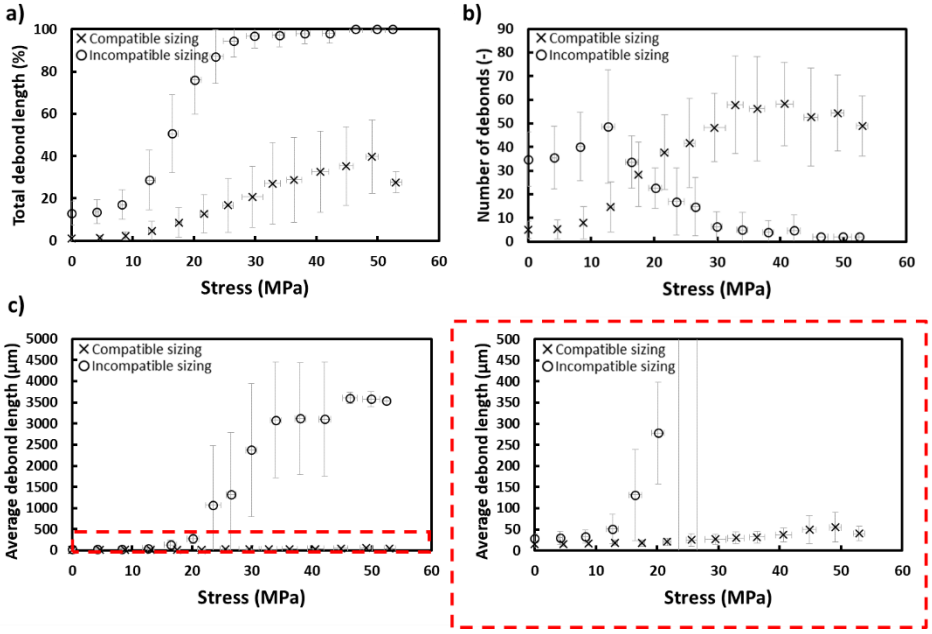

Figure 9 - (a) The total debond length (%) clearly increases earlier and faster for the incompatible sized samples. (b) The number of debonds first increases as new debonds are created and later on decreases as propagation results in coalescence of debonds. (c) The average debond length remains initially constant and starts to increase when propagation starts to take place (this happens much earlier for the incompatible sized samples).

As observed in **Figure 6**, below a certain threshold stress level no new debonds are observed. For the compatible sized samples the number of debonds stays stable up to 8.8 ± 0.1 MPa and for the incompatible sized samples up to 8.3 ± 0.6 MPa (**Figure 9b**). Once above this threshold the number of debonds starts to increase for both types of sizing (**Figure 9b**).

For the incompatible sized samples, the onset of debond initiation is almost directly accompanied by an increase in average debond length (**Figure 9c**), which suggests that the present debonds start to propagate shortly after creation. As a result, a rapid increase in total debond length is observed (**Figure 9a**). The propagation of the debonds results in the coalescence of debonds, which is reflected in a decrease in the number of debonds (**Figure 9b**), and the average debond length rapidly increases (**Figure 9c**). As observed in **Figure 6b**, the fiber has completely debonded in the longitudinal direction long before failure is observed (**Figure 9a**, 29.9 MPa).

In contrast, for the compatible sized samples, the average debond length stays relatively stable (17.5 ± 5.6 µm) after the 'initiation threshold' is passed. This confirms the

observation of **Figure 6a,** that the created debonds remain relatively stable and no or limited propagation is initially present (**Figure 9c**). Therefore, the total debond length increases much slower for the compatible sized samples as a certain level of resistance against propagation seems present (**Figure 9a**).

A similar increase in average debond length compared to the incompatible sized samples is observed at much higher stress levels (**Figure 9c**, 25.6 ± 0.9 MPa versus 12.7 ± 1.0 MPa). The later onset of propagation results in the continued increase in the number of debonds (**Figure 9b**). Only at stress levels near 40.6 ± 1.4 MPa does the number of debonds start to decrease and a larger average debond length becomes present. This increase in average debond length (**Figure 9c**) does not seem to have an influence on the increase in total debond length (**Figure 9a**) as this keeps increasing linearly. This suggests that even near the point of sample failure, the propagation of debonds is still limited for the compatible-sized samples.

The observed behaviors in the central zone of the sample (Zone 1) are also observed in Zone 2 (**Figure 10**). A delayed effect is observed as the present stress in this zone is lower than the central reference zone (**Figure 3e**). However, this similarity in trends supports the observations of the central zone.

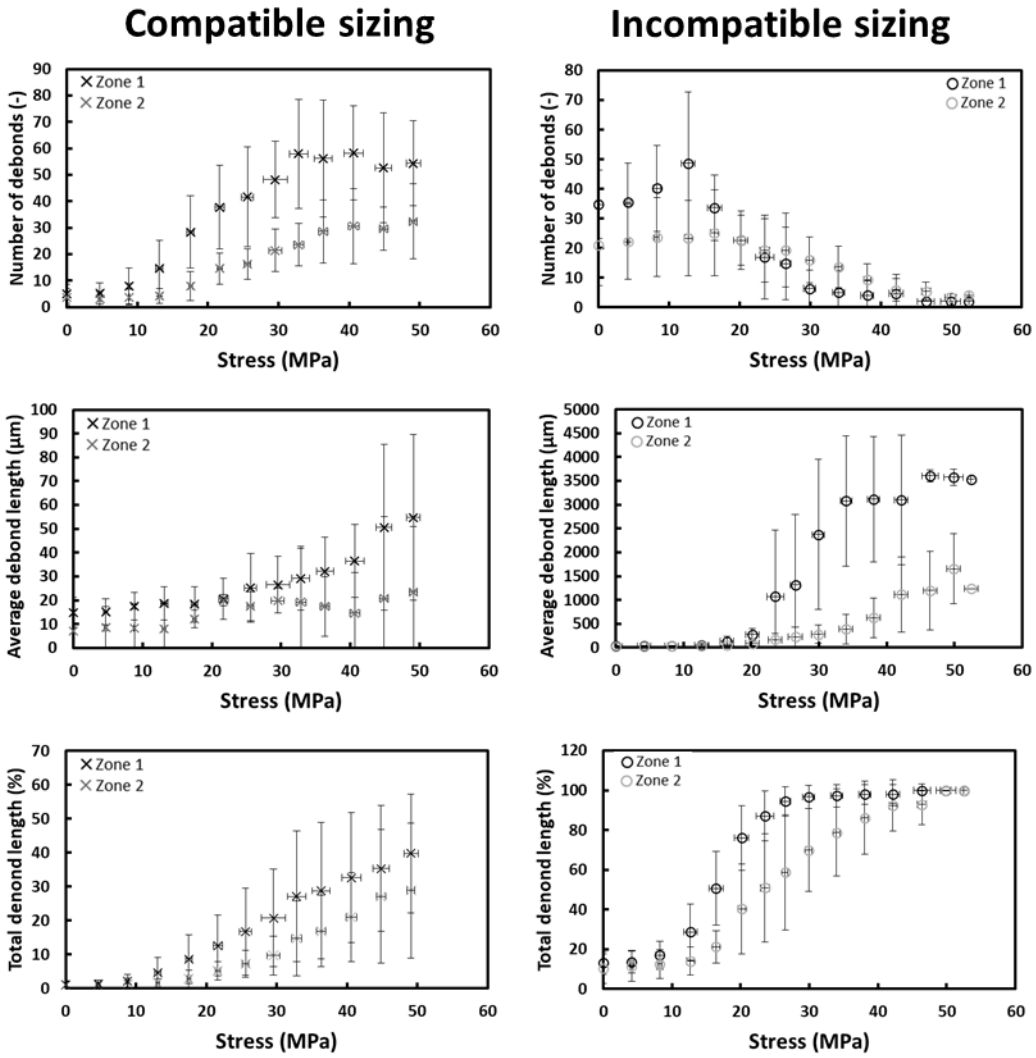

Figure 10 - The number of debonds, average debond length, and total debond length per zone for the incompatible and compatible sizing. The data is reported in reference to the stress present in zone 1. A delayed trend can be observed for all curves which can be related to the lower stress levels present at the outer sides of the gauge area.

The test observations and data analysis show that the debonding process is a combined occurrence of local debond initiations and propagations of existing debonds, rather than a sequential event of initiation and debonding propagation. The debonding process can thus be described by defining the total debond length as a function of the present stress level, $L_{debond}(\sigma)$. This function can be separated into debond lengths stemming from initiation events and debond lengths stemming from the propagation of existing debonds:

$$L_{debond}(\sigma) = L_{ini}(\sigma) + L_{prop}(\sigma) \quad (3)$$

Three different stress stages can be defined from the experimental data. Below an initiation, onset stress ($\sigma < \sigma_{ini}$) no debondings are observed (neglecting the ones occurring during production) (**Figure 11**).

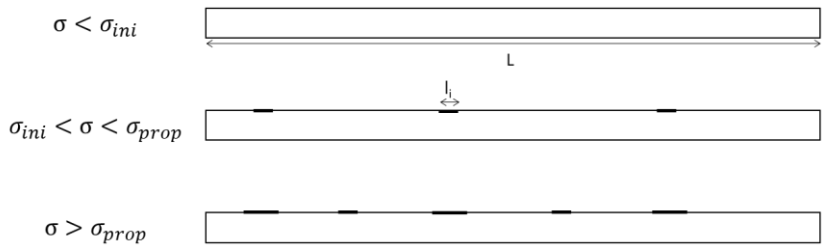

Figure 11 Schematic overview of total debond length increase which can be divided into an initiation part and propagation part.

Once the initiation threshold stress is overcome, new debonds appear ($\sigma_{ini} < \sigma < \sigma_{prop}$). The debond initiation stress can be defined as the point where the total number of debonds observed drastically increases (**Figure 9b**). Theoretically, a debond initiation happens over an infinitesimally small length. The experimental data however shows that a new initiation has a small but finite length (which is quite stable and reproducible) suggesting the presence of an average debond initiation length (**Table 2**).

Above a certain propagation threshold value ($\sigma > \sigma_{prop}$) an increase in average debond length is observed suggesting that the average debond starts to grow. During the initial stages of debond propagation (limited debond coalescence present) a linear increase in average debond length is observed, resulting in the possibility of estimating the linear debond propagation speed based on the increase in average debond length.

Table 2 - Overview of parameter values based on the available data.

Parameter	**Compatible sizing**	**Incompatible sizing**
Debond initiation onset stress	8.8 ± 0.1 MPa	8.25 ± 0.6 MPa
Average debond initiation length	15 ± 6 µm	29 ± 11 µm
Debond propagation onset stress	21.6 ± 0.7 MPa	12.7 ± 1 MPa
Debond propagation speed	0.001 mm/MPa	0.03 mm/MPa
Initial debonding length	1.2%	13.1%

The debond propagation speed for the compatible-sized samples is much lower than for the incompatible-sized samples. This shows, together with a higher debonding propagation onset stress, the better resistance of the compatible-sized samples against propagation. Since in both cases already at relatively low-stress levels debonds start to occur, the resistance against propagation seems to be the major factor in preventing fast and complete fiber-matrix failure.

The above-mentioned values are onset values above which a certain debonding phenomenon is seen. For both sizing types, it is observed that the initiation of debonds happens over a certain stress range. Especially for the compatible-sized samples this is a broad distribution as even at the point of specimen failure initiation events are still witnessed (no fully debonded interface). Therefore, it is interesting to try to fit a probability distribution through the data, estimating the probability of failure at a certain stress level. To achieve this it is assumed that before the debond propagation threshold is reached, the total debond length is purely the result of the initiation of new debonds. Thus, within this region, the total debond length at a certain stress level is assumed to be equal to the probability of debonding at that stress level due to debond initiation.

Since only a small part of the probability distribution is experimentally available (range 0 MPa to 20 MPa), both a cumulative Gaussian distribution and a cumulative Weibull distribution were fitted through the data. Both distributions are common to assess failure-related phenomena. For the compatible-sized samples, this resulted in a Gaussian distribution with an average value of 34.0 MPa and a standard deviation of 10.9 MPa. However, while these seem acceptable values, the cumulative Gaussian distribution predicts a faster total debond length increase than is actually present (**Figure 12a**).

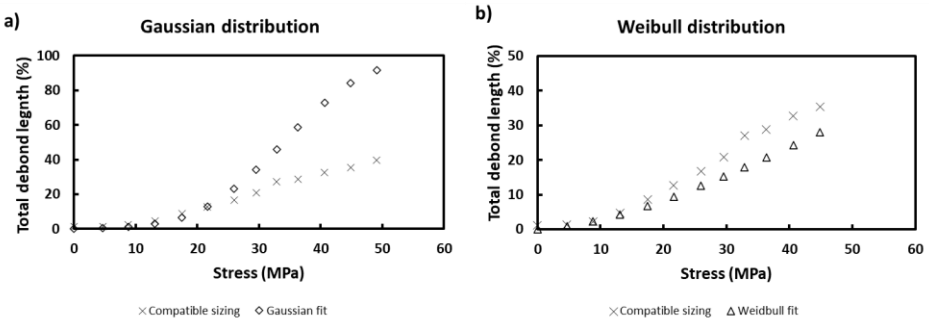

Figure 12 - (a) The cumulative Gaussian distribution fit results in a faster total debond length increase than is present in the experiments. (b) The cumulative Weibull distribution fit results in a better fit and a slower total debond length increase is predicted.

A better fit was obtained when a Weibull distribution was fitted through the data (**Figure 12b**). This resulted in a shape factor (λ) of 1.63, and a scale factor (k) of 88.5. Based on the obtained Weibull distribution an average value and standard deviation can be calculated (**Equation 4 and 5**).

$$\mu_{Weibull} = \lambda * \Gamma(1 + k_{Weibull}^{-1}) \quad (4)$$

$$\sigma_{Weibull} = \lambda * \sqrt{\Gamma\left(1 + \frac{2}{k}\right) - (\Gamma\left(1 + \frac{1}{k}\right))^2} \quad (5)$$

with Γ the gamma function. This results in an average value of 79.2 MPa with a standard deviation of 49.6 MPa. The cumulative Weibull distribution predicts a slower increase in total debond length than is actually present. This is more realistic since the total debond length is partially defined by length increase due to propagation. The large standard deviation reflects both the early observation of debonds and the partially intact interface at fracture that is observed for the compatible-sized samples. A physical explanation for this observation might be that it can be seen as a measure of the homogeneity of the sizing (application and quality): early debonds can be the result of limited or bad local sizing while the intact zones at higher stresses represent optimal sizing.

A similar fitting procedure was executed for the incompatible-sized samples. Since the data to fit the distribution is even more limited (0-12 MPa) only a Gaussian distribution could be fitted. This resulted in a Gaussian distribution with an average value of 25.0 MPa and a standard deviation of 9.2 MPa. In contrast to the Gaussian distribution for the compatible sizing, here the cumulative Gaussian distribution does predict a slower increase in total debond length than is actually present and might thus be an acceptable prediction (**Figure 13**).

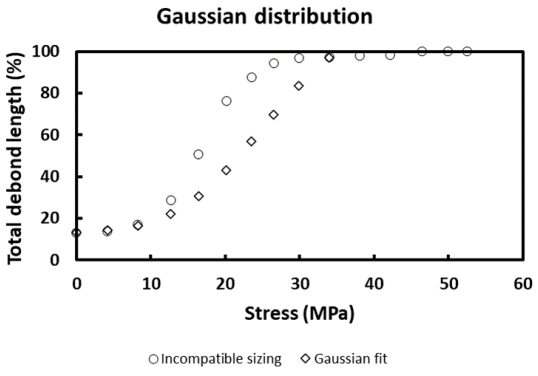

Figure 13 - The cumulative Gaussian distribution fit results in a slower total debond length increase than is present in the experimental data.

Remarkable is that the average debond initiation stress based on the Weibull or Gaussian fit is higher than the observed debond propagation onset stress threshold value. While this seems counterintuitive it needs to be taken into account that at a debond tip a local stress concentration is present. Therefore, the local stress at the debond tip will be higher than the reported 'remote' debond propagation stress level.

Table 3 - Overview of the debond initiation values based on a Gaussian and Weibull fit.

Parameter	Compatible sizing	Incompatible sizing
Debond initiation strength (Gaussian)	34.0 ± 10.9 MPa	25.0 ± 9.2 MPa
Debond initiation strength (Weibull)	79.2 ± 49.6 MPa	/

The obtained values of **Table 2 and 3** are estimations based on the assumptions that before a certain onset level no initiation and/or propagation takes place. They thus rather represent an overall behavior of the fiber-matrix interface than individual debonds. Yet, they hold value in evaluating the behavior and quality of a fiber-matrix interface. Based on the observed debonding phases and extracted data set, a descriptive formula can be constructed representing the overall failure behavior.

The debond length associated with debond initiations can be described as a function of the number of debonds present at a certain stress level, multiplied by the average debond length associated with a new initiation. Theoretically, a debond initiation happens over an infinitesimally small length. The experimental data however shows that new initiation has a small but finite length (which is quite stable and reproducible). This ratifies the use of a debond initiation length (l_{ini}).

$$L_{ini}(\sigma) = \#_{ini}(\sigma) * l_{ini} \quad (6)$$

To get the total debond length associated with debond initiations (L_{ini}), the number of debonds ($\#_{ini}$) needs to be calculated. The length over which new debonds can initiate depends on how much fiber-matrix interface length (L) is still intact. Therefore L is a function of the stress level:

$$L_j(\sigma) = L_0 - L_{debond,j-1}(\sigma) \tag{7}$$

With L_0 the initial fiber-matrix interface length.

At each increment in stress, the total amount of initiated debonds is equal to:

$$\#_{ini,j}(\sigma) = \#_{ini,j-1}(\sigma) + \frac{\int_0^{L_j(\sigma)} P_{ini,j}(\sigma) dL}{l_{ini}}$$

$$= \#_{ini,j-1}(\sigma) + \frac{(L_0 - L_{debond,j-1}(\sigma))}{l_{ini}} P_{ini,j}(\sigma) \tag{8}$$

With $P_{ini}(\sigma)$ the probability of debonding when a stress level σ_j is present.

Once created, each of the debonds can grow with further increasing stress. The obtained experimental data suggest, that depending on the used sizing, the initiated debonds almost immediately propagate (bad sizing) or stay stable for a prolonged time, and only start to grow once a certain threshold value is passed (σ_{prop}).

$$L_{prop,j}(\sigma) = \#_{ini,j} * l_{prop,j}(\sigma) \tag{9}$$

With $l_{prop,j}(\sigma)$ the propagation length for a single crack for stress increment j. The propagation length will depend on the propagation rate (mm/MPa) and number of debonds. When a constant growth rate is assumed, which seems viable from the linear increase in average crack length (**Figure 12**) during initial propagation stages (limited debond coagulation assumed), the propagation length for stress increment j becomes:

$$L_{prop,j}(\sigma) = v_{prop} * (\sigma_j - \sigma_{j-1}) \tag{10}$$

Combining all **Equation 3-8**, the total crack length at a certain stress level can be described by:

$$L_{debond,j}(\sigma) = l_{ini} * \left(\#_{ini,j-1}(\sigma) + \frac{\left(L_0 - L_{debond,j-1}(\sigma)\right)}{l_{ini}} P_{ini,j}(\sigma) \right)$$

$$+ L_{prop,j-1} + \left(\#_{ini,j-1}(\sigma) + \frac{\left(L_0 - L_{debond,j-1}(\sigma)\right)}{l_{ini}} P_{ini,j}(\sigma) \right) * v_{prop} \tag{11}$$

$$* (\sigma_j - \sigma_{j-1})$$

Below the value of σ_{ini} this formula (**Equation 11**) is reduced to a single constant value representing the amount of debond length present before loading (here assumed zero). Between σ_{ini} and σ_{prop} only the term associated with initiation is in play. While very limited growth in the individual cracks was observed it is reasonable to assume that at this stage ($\sigma_{ini} < \sigma < \sigma_{prop}$) the majority of debond length increase is due to the initiation of new debonds. Once beyond the value of σ_{prop}, debond growth starts to play a major role in the debond length growth and the complete formula will describe the total debonding length (L_{debond}).

This formula leads to five necessary parameters that are needed to describe the debonding length in function of applied stress: the length associated with a single initiation (lini), the initiation onset stress level (σ_{ini}), the initiation probability distribution (Pini(σ)), the propagation onset stress level (σ_{prop}), and the propagation growth rate. Filling in the derived data points (**Table 1 and 2**) into **Equation 11**, a descriptive function of the total debond length is obtained (**Figure 14**). This function represents accurately the overall trend of debond length growth with increased stress levels. Yet, a delayed effect seems to be present which can be due to the fact that only after the onset stress a certain phenomenon is taken into account, while in reality it has already started. However, the general assumptions and simplifications still lead to a good representation of the overall debond growth behavior.

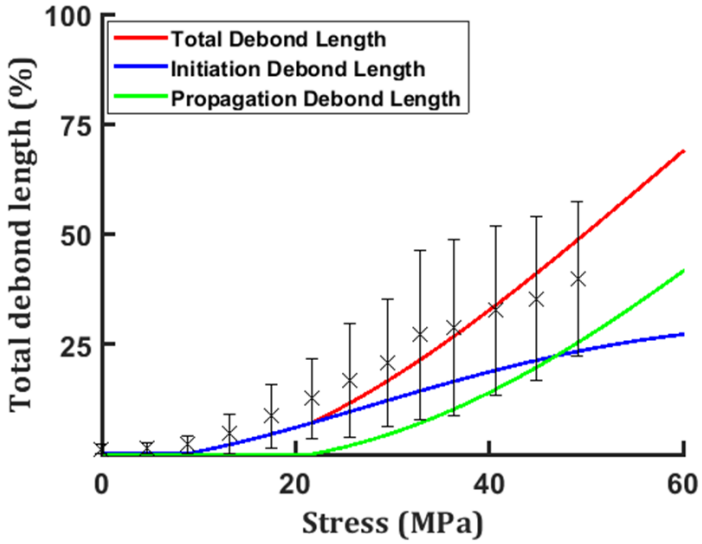

Figure 14 - Total debond length evolution based on Equation 11 (red) and the fraction of initiation debond length (blue) and propagation debond length (green). The experimental data for the compatible sized fibers is shown as well.

4. Conclusion

This paper introduces a novel method for evaluating the fiber-matrix interface under normal loading conditions using the cruciform sample design. By using a miniaturized VARI technique, high-quality samples were obtained. To prevent premature failure during testing, we enhanced the cruciform sample design by adding support sheets, creating a thin middle gauge area to localize the highest stresses at the fiber-matrix interface. This allowed us to study the fiber-matrix interface strength, even for high-quality sizings.

The combination of a step-and-shoot method with a transmission light microscope further increased the quality of the obtained data as the complete fiber-matrix interface zone could be studied in detail. Our observations differed from existing literature, where fiber-matrix debonding typically starts from a single damage site and expands. Instead, we observed the initiation of numerous small debonds across the fiber-matrix interface zone. These many small debonds grew and coalesced upon stress increase, forming larger fiber-matrix debonds. The use of polarized light revealed stress concentrations at the debond tips as well as the creation of plastic deformation bands around the debonded zones.

The step-and-shoot method allowed us to monitor and analyze the development of individual debonds in function of far-field stress levels. We found that for both good and bad sizing, fiber-matrix debonds initiated at far-field stress levels exceeding 8.7 MPa.

Once debonds started to initiate, large differences between both sizings were observed. In the case of incompatible sizing, debonds quickly grew beyond 12.7 ± 1.0 MPa far-field stress, whereas compatible-sized fibers experienced only initiation, with minimal growth until much higher far-field stress levels (above 40.6 ± 1.4 MPa). At the point of failure, the incompatible-sized fiber is completely debonded, while compatible-sized samples contain a large collection of debonds at the interface. As a result, the incompatible-sized fiber samples failed at the debonded fiber-matrix interface, while the compatible-sized fiber samples failed at the edge of the thinned middle section.

The obtained data plots for total debond length, average debond length, and number of debonds illustrate these trends. Based on these trends a simplified predictive formula for the total debond length was derived. Nonetheless the simplifications, the obtained formula showed good agreement with the experimental data.

Our newly presented production and testing methodology for cruciform-shaped samples shows promise for studying fiber-matrix interface debonding. With a limited number of tests, we can gain valuable insights into the debonding process. The ability to construct a simplified predictive formula for total debond length based on these cost-effective tests holds potential for both industrial evaluation of sizing and application procedures and computer-aided simulations of composite failure behavior.

5. Acknowledgements

This work was supported by the Special Research Fund of Ghent University [grant number: BOF/STA/202009/046, BOF/24J/2023/006].

6. Data availability

The raw/processed data required to reproduce these findings cannot be shared at this time as the data is part of an ongoing study.

7. Bibliography

[1] F.A. Gilabert, D. Garoz, R.D.B. Sevenois, S.W.F. Spronk, A. Rezaei, W. Van Paepegem, Composite micro-scale model accounting for debonding, strain rate-dependence and damage under impact using an explicit finite element solver, ECCM 2016 - Proceeding of the 17th European Conference on Composite Materials (2016) 26–30.

[2] T.J. Vaughan, C.T. McCarthy, Micromechanical modelling of the transverse damage behaviour in fibre reinforced composites, Composites Science and Technology 71 (2011) 388–396. https://doi.org/10.1016/j.compscitech.2010.12.006.

[3] W. Tan, F. Naya, L. Yang, T. Chang, B.G. Falzon, L. Zhan, J.M. Molina-Aldareguía, C. González, J. Llorca, The role of interfacial properties on the intralaminar and interlaminar damage behaviour of unidirectional composite laminates: Experimental characterization and multiscale modelling, Composites Part B: Engineering 138 (2018) 206–221. https://doi.org/10.1016/j.compositesb.2017.11.043.

[4] M. fa Ren, X. wen Zhang, C. Huang, B. Wang, T. Li, An integrated macro/micro-scale approach for in situ evaluation of matrix cracking in the polymer matrix of cryogenic composite tanks, Composite Structures 216 (2019) 201–212. https://doi.org/10.1016/j.compstruct.2019.02.079.

[5] D.A. Jesson, J.F. Watts, The Interface and Interphase in Polymer Matrix Composites: Effect on Mechanical Properties and Methods for Identification, Http://Dx.Doi.Org/10.1080/15583724.2012.710288 52 (2012) 321–354. https://doi.org/10.1080/15583724.2012.710288.

[6] J.D.H. Hughes, The carbon fibre/epoxy interface—A review, Compos Sci Technol 41 (1991) 13–45. https://doi.org/10.1016/0266-3538(91)90050-Y.

[7] P.J. Herrera-Franco, L.T. Drzal, Comparison of methods for the measurement of fibre/matrix adhesion in composites, Composites 23 (1992) 2–27. https://doi.org/10.1016/0010-4361(92)90282-Y.

[8] J. Koyanagi, S. Ogihara, H. Nakatani, T. Okabe, S. Yoneyama, Mechanical properties of fiber/matrix interface in polymer matrix composites, Https://Doi.Org/10.1080/09243046.2014.915125 23 (2014) 551–570. https://doi.org/10.1080/09243046.2014.915125.

[9] S. Huang, Q. Fu, L. Yan, B. Kasal, Characterization of interfacial properties between fibre and polymer matrix in composite materials – A critical review, Journal of Materials Research and Technology 13 (2021) 1441–1484. https://doi.org/10.1016/J.JMRT.2021.05.076.

[10] Z. Liu, X. Yuan, A.J. Beck, F.R. Jones, Analysis of a modified microbond test for the measurement of interfacial shear strength of an aqueous-based adhesive and a polyamide fibre, Compos Sci Technol 71 (2011) 1529–1534. https://doi.org/10.1016/J.COMPSCITECH.2011.06.001.

[11] M. Nishikawa, T. Okabe, K. Hemmi, N. Takeda, Micromechanical modeling of the microbond test to quantify the interfacial properties of fiber-reinforced composites, Int J Solids Struct 45 (2008) 4098–4113. https://doi.org/10.1016/J.IJSOLSTR.2008.02.021.

[12] L. Yu, K. Wang, Y. Guan, Z. Liu, M. Sun, Y. Zhao, Effect of carbon fiber surface properties on carbon fiber/polyphenylene sulfide composite interfacial property, Polym Compos 44 (2023) 2005–2015. https://doi.org/10.1002/PC.27224.

[13] M.R. Piggott, Why interface testing by single-fibre methods can be misleading, Compos Sci Technol 57 (1997) 965–974. https://doi.org/10.1016/S0266-3538(97)00036-5.

[14] L. Yang, J.L. Thomason, Interface strength in glass fibre–polypropylene measured using the fibre pull-out and microbond methods, Compos Part A Appl Sci Manuf 41 (2010) 1077–1083. https://doi.org/10.1016/J.COMPOSITESA.2009.10.005.

[15] S.F. Zhandarov, E. V. Pisanova, The local bond strength and its determination by fragmentation and pull-out tests, Compos Sci Technol 57 (1997) 957–964. https://doi.org/10.1016/S0266-3538(97)00037-7.

[16] J.M. Park, J.W. Kim, D.J. Yoon, Comparison of Interfacial Properties of Electrodeposited Single Carbon Fiber/Epoxy Composites Using Tensile and Compressive Fragmentation Tests and Acoustic Emission, J Colloid Interface Sci 247 (2002) 231–245. https://doi.org/10.1006/JCIS.2001.8135.

[17] X.F. Zhou, H.D. Wagner, S.R. Nutt, Interfacial properties of polymer composites measured by push-out and fragmentation tests, Compos Part A Appl Sci Manuf 32 (2001) 1543–1551. https://doi.org/10.1016/S1359-835X(01)00018-5.

[18] S. Keusch, H. Queck, K. Gliesche, Influence of glass fibre/epoxy resin interface on static mechanical properties of unidirectional composites and on fatigue performance of cross ply composites, Compos Part A Appl Sci Manuf 29 (1998) 701–705. https://doi.org/10.1016/S1359-835X(97)00106-1.

[19] P.S. Chua, M.R. Piggott, The glass fibre—polymer interface: I—theoretical consideration for single fibre pull-out tests, Compos Sci Technol 22 (1985) 33–42. https://doi.org/10.1016/0266-3538(85)90089-2.

[20] J.C. Zarges, H.P. Heim, Influence of cyclic loads on the fiber-matrix-interaction of cellulose and glass fibers in polypropylene, Compos Part A Appl Sci Manuf 149 (2021) 106491. https://doi.org/10.1016/J.COMPOSITESA.2021.106491.

[21] C. Ageorges, K. Friedrich, T. Schüller, B. Lauke, Single-fibre Broutman test: Fibre-matrix interface transverse debonding, Compos Part A Appl Sci Manuf 30 (1999) 1423–1434. https://doi.org/10.1016/S1359-835X(99)00045-7.

[22] T. Schüller, W. Beckert, B. Lauke, C. Ageorges, K. Friedrich, Single fibre transverse debonding: stress analysis of the Broutman test, Compos Part A Appl Sci Manuf 31 (2000) 661–670. https://doi.org/10.1016/S1359-835X(00)00034-8.

[23] T. Schüller, W. Beckert, B. Lauke, K. Friedrich, Single-fibre transverse debonding: tensile test of a necked specimen, Compos Sci Technol 60 (2000) 2077–2082. https://doi.org/10.1016/S0266-3538(00)00100-7.

[24] R. Sinclair, R.J. Young, R.D.S. Martin, Determination of the axial and radial fibre stress distributions for the Broutman test, Compos Sci Technol 64 (2004) 181–189. https://doi.org/10.1016/S0266-3538(03)00257-4.

[25] K. Martyniuk, B.F. Sørensen, P. Modregger, E.M. Lauridsen, 3D in situ observations of glass fibre/matrix interfacial debonding, Compos Part A Appl Sci Manuf 55 (2013) 63–73. https://doi.org/10.1016/J.COMPOSITESA.2013.07.012.

[26] R. Livingston, B. Koohbor, Characterizing fiber-matrix debond and fiber interaction mechanisms by full-field measurements, Composites Part C: Open Access 7 (2022) 100229. https://doi.org/10.1016/J.JCOMC.2022.100229.

[27] M. Fichera, K. Totten, L.A. Carlsson, Seawater effects on transverse tensile strength of carbon/vinylester as determined from single-fiber and macroscopic specimens, J Mater Sci 50 (2015) 7248–7261. https://doi.org/10.1007/S10853-015-9279-3/TABLES/9.

[28] K.R. Totten, B. Kutub, L.A. Carlsson, In situ determination of the fiber–matrix interface tensile strength, Http://Dx.Doi.Org/10.1177/0021998315579926 50 (2015) 589–599. https://doi.org/10.1177/0021998315579926.

[29] H. Zhang, M.L. Ericson, J. Varna, L.A. Berglund, Transverse single-fibre test for interfacial debonding in composites: 1. Experimental observations, Compos Part A Appl Sci Manuf 28 (1997) 309–315. https://doi.org/10.1016/S1359-835X(96)00123-6.

[30] D.B. Gundel, B.S. Majumdar, D.B. Miracle, Evaluation of the transverse response of fiber-reinforced composites using a cross-shaped sample geometry, Scripta Metallurgica et Materialia 33 (1995) 2057–2065. https://doi.org/10.1016/0956-716X(95)00459-9.

[31] G.P. Tandon, R.Y. Kim, V.T. Bechel, Fiber–Matrix Interfacial Failure Characterization Using a Cruciform-Shaped Specimen, Http://Dx.Doi.Org/10.1177/002199802761675575 36 (2002) 2667–2691. https://doi.org/10.1177/002199802761675575.

[32] J. Koyanagi, S. Ogihara, Temperature dependence of glass fiber/epoxy interface normal strength examined by a cruciform specimen method, Compos B Eng 42 (2011) 1492–1496. https://doi.org/10.1016/J.COMPOSITESB.2011.04.041.

[33] J.M. Chu, B. Claus, B.H. Lim, D. O'Brien, T. Sun, K. Fezzaa, W. Chen, Rate effects on fiber–matrix interfacial transverse debonding behavior, J Compos Mater 54 (2020) 501–517.

655 https://doi.org/10.1177/0021998319866904/ASSET/IMAGES/LARGE/10.1177_0021998
656 319866904-FIG18.JPEG.
657 [34] J. Koyanagi, H. Nakatani, S. Ogihara, Comparison of glass–epoxy interface strengths
658 examined by cruciform specimen and single-fiber pull-out tests under combined stress
659 state, Compos Part A Appl Sci Manuf 43 (2012) 1819–1827.
660 https://doi.org/10.1016/J.COMPOSITESA.2012.06.018.
661 [35] G.P. Tandon, R.Y. Kim, V.T. Bechel, Construction of the Fiber-Matrix Interfacial Failure
662 Envelope in a Polymer Matrix Composite, Int J Multiscale Comput Eng 2 (2004) 13.
663 https://doi.org/10.1615/INTJMULTCOMPENG.V2.I1.70.
664 [36] V.T. Bechel, G.P. Tandon, Modified Cruciform Test for Application to Graphite/Epoxy
665 Composites, Http://Dx.Doi.Org/10.1080/153764902317224842 9 (2010) 1–17.
666 https://doi.org/10.1080/153764902317224842.
667 [37] D.C. Foster, G.P. Tandon, M. Zoghi, Evaluation of failure behavior of transversely loaded
668 unidirectional model composites, Exp Mech 46 (2006) 217–243.
669 https://doi.org/10.1007/S11340-006-6413-9/METRICS.
670 [38] B.S. Majumdar, D.B. Gundel, R.E. Dutton, S.G. Warrier, N.J. Pagano, Evaluation of the
671 Tensile Interface Strength in Brittle-Matrix Composite Systems, Journal of the American
672 Ceramic Society 81 (1998) 1600–1610. https://doi.org/10.1111/J.1151-
673 2916.1998.TB02522.X.
674 [39] S. Levine, Y. Nie, W. Chen, Dynamic Transverse Debonding of a Single Fiber, Journal of
675 Dynamic Behavior of Materials 2 (2016) 521–531. https://doi.org/10.1007/s40870-016-
676 0086-y.
677 [40] K. Allaer, I. De Baere, W. Van Paepegem, J. Degrieck, Direct fracture toughness
678 determination of a ductile epoxy polymer from digital image correlation measurements
679 on a single edge notched bending sample, Polymer Testing 42 (2015) 199–207.
680 https://doi.org/10.1016/j.polymertesting.2015.01.014.
681 [41] M. Merzlyakov, G.B. McKenna, S.L. Simon, Cure-induced and thermal stresses in a
682 constrained epoxy resin, Composites Part A: Applied Science and Manufacturing 37
683 (2006) 585–591. https://doi.org/10.1016/J.COMPOSITESA.2005.05.013.
684 [42] Q. Li, C.E. Weinell, S. Kiil, Curing-induced internal stress in epoxy coatings: Effects of
685 epoxy binder, curing agent, filler, initial solvent concentration, curing temperature, and
686 relative humidity, Progress in Organic Coatings 173 (2022) 107175.
687 https://doi.org/10.1016/J.PORGCOAT.2022.107175.
688 [43] N. Lorenz, M. Müller-Pabel, J. Gerritzen, J. Müller, B. Gröger, D. Schneider, K. Fischer,
689 M. Gude, C. Hopmann, Characterization and modeling cure- and pressure-dependent

thermo-mechanical and shrinkage behavior of fast curing epoxy resins, Polymer Testing 108 (2022) 107498. https://doi.org/10.1016/J.POLYMERTESTING.2022.107498.

[44] E. Ruiz, F. Trochu, Numerical analysis of cure temperature and internal stresses in thin and thick RTM parts, Composites Part A: Applied Science and Manufacturing 36 (2005) 806–826. https://doi.org/10.1016/J.COMPOSITESA.2004.10.021.

[45] C. Kim, S.P. Phansalkar, H.S. Lee, B. Han, Measurement of effective cure shrinkage of epoxy-based molding compound by fiber Bragg grating sensor using two-stage curing process, Journal of Applied Polymer Science 139 (2022) 51620. https://doi.org/10.1002/APP.51620.

[46] M. Nikforooz, O. Verschatse, L. Daelemans, K. De Clerck, W. Van Paepegem, Mixed experimental-numerical method for quantitative measurement of mode II fibre/matrix interface debonding and comparison of fibre sizings in single short fibre composites, Polym Test 134 (2024) 108435. https://doi.org/10.1016/J.POLYMERTESTING.2024.108435.

[47] M. Nikforooz, O. Verschatse, L. Daelemans, K. De Clerck, W. Van Paepegem, Experimental method for in-situ real-time measurement of mixed mode fibre/matrix interface debonding and comparison of fibre sizings in single short fibre composites, Compos Sci Technol 249 (2024) 110488. https://doi.org/10.1016/J.COMPSCITECH.2024.110488.